Chemical synthesis and characterization of a new quinazolinedione competitive antagonist for strigolactone receptors with an unexpected binding mode

Cyril Hamiaux[1*], Lesley Larsen[3,†], Hui Wen Lee[1,2], Zhiwei Luo[1], Prachi Sharma[1,2], Bill C. Hawkins[3], Nigel B. Perry[3,4], Kimberley C. Snowden[1]

[1]The New Zealand Institute for Plant and Food Research Limited, Auckland, New Zealand

[2]University of Auckland, School of Biological Sciences, Auckland, New Zealand

[3]Department of Chemistry, University of Otago, Dunedin, New Zealand

[4]The New Zealand Institute for Plant and Food Research Limited, Department of Chemistry, University of Otago, Dunedin, New Zealand

*Corresponding author: cyril.hamiaux@plantandfood.co.nz

†Died 28 April 2018. We dedicate this paper to Lesley, in memory of her great enthusiasm and her relentless pursuit of synthetic targets.

Abstract

Strigolactones are multifunctional plant hormones regulating essential physiological processes affecting growth and development. In vascular plants, strigolactones are recognized by α/β hydrolase fold proteins from the D14/DAD2 family in the initial step of the signalling pathway. We have previously discovered that *N*-phenylanthranilic acid derivatives (e.g. tolfenamic acid) are potent antagonists of strigolactone receptors, prompting us to design quinazolinone and quinazolinedione derivatives (QADs and QADDs, respectively) as second-generation antagonists. Initial *in silico* docking studies suggested that these compounds would bind to DAD2, the petunia strigolactone receptor, with higher affinity than the first-generation compounds. However, only one of the QADs/QADDs tested in *in vitro* assays acted as a competitive antagonist of strigolactone receptors, with reduced affinity and potency compared with its *N*-phenylanthranilic acid "parent". X-ray crystal structure analysis revealed that the binding mode of the active QADD inside DAD2's cavity was not that predicted *in silico*, highlighting a novel inhibition mechanism for strigolactone receptors. Despite a ~10-fold difference in potency *in vitro*, the QADD and tolfenamic acid had comparable activity *in planta*, suggesting that the QADD compensates for lower potency with increased bioavailability. Altogether, our results establish this QADD as a novel lead compound towards the development of potent and bioavailable antagonists of strigolactone receptors.

Abbreviations list

SL, strigolactone ; QAD quinazolinone derivative ; QADD, quinazolinedione derivative ; MNAB, 2-(2'-methyl-3'-nitroanilino)benzoic acid; DSF, differential scanning fluorimetry; YLG, Yoshimulactone green; DMF, *N,N*-Dimethylformamide

Introduction

Strigolactones (SLs) are carotenoid-derived compounds that affect a large variety of developmental and physiological responses across the plant kingdom. In vascular plants, these compounds act as endogenous hormones to regulate processes such as shoot branching, root development, leaf senescence, and abiotic stress response (1-8). SLs are also exuded from the roots of plants to the rhizosphere where they mediate interactions with symbiotic arbuscular mycorrhizal fungi (9) and with the *Striga*, *Phelipanche* and *Orobanche* parasitic weeds (10-13).

Details of SL biosynthesis, perception and signalling are now well understood, particularly in model plants (see (14) for a recent review), and α/β hydrolase-fold proteins from the Decreased Apical Dominance 2/Dwarf14 (DAD2/D14) clade have been identified as SL receptors in the first step of the SL signalling pathway (13, 15-19). Unexpectedly for a receptor, these proteins still have low, but absolutely essential, hydrolase activity towards their hormone substrate that results in the cleavage of a bond between the ABC tricyclic lactone part of SL molecule and the conserved butenolide moiety (D ring) (16, 19). During catalysis, a covalent intermediate is formed between the D ring and the histidine residue of the catalytic triad of the receptor, probably explaining the very slow rate of hydrolysis (15, 18). Binding and hydrolysis of the SL hormone triggers a large conformational change in the lid domain of the receptor, allowing its interaction with More Axillary Growth 2 (MAX2) protein from a Skp-Cullin-Fbox (SCF) protein complex (18, 19). SL receptors also show SL-dependent interactions with repressor proteins of SL signalling belonging to the D53/Suppressor of MAX2-like (SMXL) family to probably recruit them to the SCF complex (17, 20, 21). Following polyubiquitination by the SCF complex, the D53/SMXL repressor

proteins are targeted to the 26S proteasome for degradation, resulting in a transcriptional response to the presence of the hormone signal.

SL receptors have a classical α/β hydrolase fold, consisting of a 7-stranded β-sheet "core" domain flanked by 7 α helices. A lid, consisting of four additional helices inserted between β5 and α9 of the "core" domain, caps the core domain over a large central cavity harbouring the serine and histidine residues from the catalytic triad, as well as phenylalanine residues particularly conserved across members of the DAD2/D14 clade (16, 19, 22-28). These observations rapidly led to the hypothesis that SL receptors are "druggable" and that the SL signalling pathway could therefore be manipulated by chemical factors to provide novel plant growth regulators affecting plant architecture (29). In line with this hypothesis, eight compound classes have recently been described as antagonists of SL receptors with various affinities, potencies and *in planta* effects (reviewed in (30)): soporidine (31), 2-methoxy-1-naphthaldehyde (32), β-lactones (33), DL1 (34), *N*-phenylanthranilic acid derivatives (35),Triton X-100 (36), carba-SLs (37) and 1,2,3- triazole ureas (38).

The mode of action of *N*-phenylanthranilic acid derivatives has been characterized at the structural level (35). In the co-crystal structures of petunia DAD2 with tolfenamic acid and the related 2-(2'-methyl-3'-nitroanilino)benzoic acid (MNAB), and of rice D14 with MNAB, the antagonists were found to fully occupy the binding cavity with excellent shape complementarities. The binding mode of these compounds to the petunia and rice SL receptors is conserved, with only very minor variations seen in the respective conformations of the bound compounds in the rice *vs* petunia receptor to account for the three amino acid differences observed in the binding cavities of these two proteins. Overall, *N*-phenylanthranilic acid derivatives bind through a combination of electrostatic and

hydrophobic interactions. In particular, the carboxylic group of the antagonists anchors the compound deep inside the cavity through electrostatic interactions with the serine and histidine residues of the catalytic triad. Furthermore, an additional hydrogen bond is observed between the antagonists and Ser219 in DAD2 (Ser270 in rice D14). This residue, strictly conserved among members of the DAD2/D14 clade, sits at the tip of the so-called activation loop that defines the entrance of the internal cavity. In the crystal structure of D14 bound to D3 (the MAX2 orthologue in rice) the lid domain of the receptor has undergone large conformational changes to interact with D3 and the activation loop is completely disordered, suggesting that GR24-induced displacement of the activation loop may unlock the lid and activate the receptor. The interaction between *N*-phenylanthranilic acid derivatives and Ser219 supported this hypothesis where, by locking the activation loop in its ground (inactive) state, the antagonists prevent the opening of the lid and activation of the receptor.

A structure-activity relationship (SAR) study using 119 *N*-phenylanthranilic acid derivatives, and 19 heteroanalog 2-phenoxybenzoic acid derivatives, suggested that the core pharmacophore is *N*-(2-methylphenyl)anthranilic acid (Figure 1a), with possible substituents to be located on positions 3–5 of the Y ring (35) (ring labels are defined on Figure 1). The requirement for unsubstituted positions on the X ring, not unexpected given the tight steric constraints around that ring in the binding pocket, may also reflect a need to maximize internal hydrogen bonding by minimizing ring twist (Figure 1b). In the present study, we tested this hypothesis by designing a series of fused compounds related to 1-phenylquinazoline-2,4(1H,3H)-dione (Figure 1b-c) and assaying their ability to act as antagonists for SL receptors using biochemical, structural and *in planta* methods.

Experimental

Materials

Compounds **0**, **5–8** were purchased from Molport (catalogue numbers: 003-809-289, 009-014-741, 002-817-647, 003-802-463 and 003-802-462, respectively), compound **10** was purchased from Sigma-Aldrich (catalogue number T0535) and compound **9** was obtained from William A. Denny (Auckland Cancer Society Research Centre).

Chemical syntheses

1-(3-Nitro-4-hydroxyphenyl)-1H-quinazoline-2,4-dione (**2**)

A solution of 1-(2-bromobenzoyl)-3-(3-nitrophenyl)-urea (250 mg, 0.68 mmol; the chemical synthesis of the intermediate urea is described in the Supplementary Experimental section) and freshly resublimed potassium *tert* butoxide (450 mg) in dry *N,N*-dimethylformamide (DMF) (7 mL) was stirred at 75°C for 2.25 h. The mixture was cooled then poured onto aq. HCl (0.5 M, 50 mL). The pale brown solid was filtered off, washed with water then dried to give the crude product. Purification by column chromatography over silica gel eluting with dichloromethane to ethyl acetate (0 to 50%) gave starting material, an unknown byproduct and the title compound (9 mg). The identity of the title compound was shown by X-ray crystallography. HRMS-ESI $[M-H]^-$ calcd for $C_{14}H_8N_3O_5$: 298.0469, Found: 298.0489. ^1H and ^{13}C NMR data are presented in Supplementary Table 1.

1-(3-Chloro-2-methylbenzyl)-1H-quinazoline-2,4-dione (**3**)

A solution of 1-(2-bromobenzoyl)-3-(3-chloro-2-methylphenyl)-urea (250 mg, 0.68 mmol; Supplementary Experimental section) and freshly resublimed potassium tert.butoxide (250 mg, 2 mmol) in dry DMF (5 mL) was heated to 70°C for 18 h. The mixture was cooled then

poured onto aq. HCl (0.5 M, 50 mL). The pale brown solid was filtered off, washed with water then dried to give the crude product. Purification by column chromatography over silica gel eluting with dichloromethane to ethyl acetate (0 to 50%) gave the pure product as a white solid (115 mg, 60%).

Microanalysis calcd for $C_{15}H_{11}ClN_2O_2$: C, 62.84; H, 3.87; N, 9.77. Found: C, 62.82; H, 3.99; N, 9.61. HRMS-ESI $[M+Na]^+$ calcd for $C_{15}H_{11}ClN_2NaO_2$: 309.0401, found: 309.0384. ^1H and ^{13}C NMR data are presented in Supplementary Table 1.

1-(3-Chlorophenyl)-1H-quinazoline-2,4-dione (**4**)

A solution of 1-(2-bromobenzoyl)-3-(3-chlorophenyl)-urea (250 mg, 0.68 mmol; Supplementary Experimental section) and freshly resublimed potassium *tert* butoxide (250 mg, 2 mmol) in dry DMF (5 mL) was heated to 70°C for 18 h. The mixture was cooled then poured onto aq. HCl (0.5 M, 50 mL). The pale brown solid was filtered off, washed with water then dried to give the crude product. Purification by column chromatography over silica gel eluting with dichloromethane to ethyl acetate (0 to 50%) gave the pure product as a white solid (165 mg, 85%).

Microanalysis calcd for $C_{14}H_9ClN_2O_2$: C, 61.67; H, 3.33; N, 10.27. Found: C, 61.57; H, 3.36; N, 10.16. HRMS-ESI $[M+Na]^+$ calcd for $C_{14}H_9ClN_2NaO_2$: 295.0245, Found: 295.0223. ^1H and ^{13}C NMR data are presented in Supplementary Table 1.

Protein expression, purification, crystallization and structure determination

Protocols for expression and purification of wt-DAD2 (for *in vitro* assays) and $DAD2_{Cys89Gln}$ (for crystallization) have previously been described (35). The Cys89Gln mutation was

introduced to prevent intermolecular covalent bond formation between cysteine residues of different monomers, and allowed the formation of diffracting crystals reproducibly. This mutation has been checked to have no effect on the *in vitro* activity of the protein (35). Prior to crystallization $DAD2_{Cys89Gln}$ was buffer exchanged into 20 mM Tris, pH 8.0, 150 mM NaCl using a Superdex 200 10/300 GL column (GE Healthcare) and concentrated to ~6.5 mg/mL. $DAD2_{Cys89Gln}$ was incubated with QADD **2** (1.25 mM, i.e. ~6x molar excess) in 20 mM Tris, pH 8.0, 150 mM NaCl, 2% DMSO for 30 min at 18°C before crystallization. Drops consisted of 1 µL of protein solution and 1 µL of reservoir solution consisting of 0.1 M Tris-Acetate, pH 8.5, 31% PEG 3350, 0.2 M $MgCl_2$. Crystals were cryo-protected by successive transfer to a reservoir solution containing 10%, 15% and 20% glycerol. A full dataset was collected at the Australian Synchrotron MX1 beamline to 1.63 Å resolution. Data were processed with iMOSFLM (39) and pointless/aimless (40). Structure determination was achieved using programs from the CCP4 package (41). The structure was solved by molecular replacement using the DAD2 structure (PDB entry code 4DNP) as starting models in Phaser (42). Refinement cycles were carried out using Refmac5 (43) and Coot (44). Restraint parameters for QADD **2** were obtained from JLigand (45). Optimized refinement parameters obtained from the PDB_redo server (46) were used in the final stages of refinement. Data collection and refinement statistics are listed in Table 1.

Docking

3D coordinates for compounds were generated in JLigand (45) from the CCP4 package, and pdb files were subsequently converted in pdbqt format using OpenBabel (47). The DAD2 "empty" structures (either the DAD2 structure bound to tolfenamic acid, PDB entry code 6AP6, or the DAD2 structure bound to QADD **2**, where the bound compounds have been

removed) were prepared in AutoDockTools (48) and used as receptors. Docking was performed in Autodock Vina (49) using a 25x25x25Å^3 box centred on the oxygen atom of Ser96. The maximum number of binding modes to be generated was set to nine.

Differential Scanning Fluorimetry

The differential scanning fluorimetry (DSF) experiments were performed as previously described (16). DAD2 was first buffer exchanged into PBS using Superdex 75 10/300 GL (GE Healthcare). 0.5 µl of compounds (10 mM in DMSO) were manually dispensed in a 384-well plate. 18.5 µL of a solution containing 6.65 µM DAD2, SyproTangerine 10.25x in PBS were added to each compound using a BIOMEK 3000 pipetting robot (Beckman Coulter) to yield a final 19 µL reaction consisting of 6.48 µM DAD2, SyproTangerine 10x, 263 µM compound, 2.6% DMSO in PBS. Reactions were incubated for 30 minutes at 18°C in the absence of light before DSF analysis.

Yeast two-hybrid assay

Yeast two-hybrid experiments were performed following methods from the Clontech Yeast Protocols Handbook, 2009, using yeast PJ69-4 (50), with DAD2 cloned into pBD vector (51), and MAX2A and D53A cloned into pAD vector (51). The presence of the binding domain and activation domain fusion proteins in selected diploid yeast strains was confirmed by Western analysis (35). Liquid culture assays using orthonitrophenyl-β-galactopyranoside (Sigma-Aldrich) as the substrate, were used to quantify the strength of the interactions between DAD2 and target proteins. DAD2/MAX2A and DAD2/D53A interactions were detected in the presence of 5 and 1 µM GR24, respectively, and compared with DMSO controls. Each inhibitor was tested at 0.1, 1, and 10x molar ratios compared with GR24.

Intrinsic fluorescence assay

Experiments were performed on a FLUOStar Omega (BMG LabTech) using 280 ± 10 nm excitation filter and 340 ± 10 nm emission filters. The gain was set to 1800 and the number of flashes to 50. Compound stocks were prepared at 10x final concentration in 20 mM Tris pH 8.0, 150 mM NaCl, 20% DMSO. DAD2 was buffer exchanged in 20 mM Tris, pH 8.0, 150 mM NaCl using gel filtration (Superdex 75 10/300 GL, GE Healthcare) and its concentration was adjusted to 11.11 µM. For experiments, 10 µL of compounds were manually dispensed and then mixed with either 90 µL buffer or 90 µL DAD2 protein solution in flat-bottomed, black 96-well plates using a BIOMEK 3000 robot (Beckman Coulter). Final protein concentration was 10 µM, with compounds ranging from 0 to 200 µM in 20 mM Tris, pH 8.0, 150 mM NaCl, 2% DMSO. All experiments (protein and buffer alike) were performed in triplicate. The plate was incubated for 30 min at 25°C before measurements. Binding curves were obtained by plotting the relative fluorescence ($|\Delta F|/F_0$) *vs* compound concentration, where F_0 is the fluorescence of the DMSO control, and $|\Delta F| = |F - F_0|$. GraphPad Prism was used to perform non-linear regressions and determine the binding constants (K_d values) using the One site – Specific Binding model.

Enzymatic inhibition assays

Experiments were performed on a FLUOStar Omega (BMG LabTech) using 485 ± 12 nm excitation filter and 520 ± 10 nm emission filters. The temperature was set to 25°C and the gain was set to 920. Measurements were performed in black 96-well plates at 2-min intervals, with 20 flashes per cycle, over 90 min. Reactions were performed at seven Yoshimulactone Green (YLG) concentrations (0, 0.2, 0.4, 0.6, 1, 2, 3.5 µM) and six inhibitor concentrations (0, 0.1, 0.5, 1, 5, 10 µM). In all cases, the protein concentration was 0.34 µM

and the reaction buffer was 20 mM Tris/HCl, pH 8.0, 150 mM NaCl, 1% DMSO. All experiments were performed in triplicate. YLG-only controls were measured in the same buffer. Fluorescent units were converted to fluorescein concentrations using fluorescein standard curves. Michaelis-Menten analyses were performed by non-linear regression in GraphPad Prism using the YLG series in the absence of inhibitor at 16-min. For inhibition kinetics, global non-linear regression analyses were performed in GraphPad Prism using a competitive inhibition model.

Plant method

Arabidopsis bud assays were performed as previously described (16). Sections of stems containing two buds were harvested from bolting plants. Treatments were applied to the base of the stems and contained 2% DMSO in 0.5x HSS (16). Treatments comprised 0.5 µM GR24 and/or 5 µM tolfenamic acid and/or 5 µM QADD **2**. After 5 days, bud length from both nodes was measured and normalized to the mock control.

Results and discussion

Initial docking study

We previously showed that docking of tolfenamic acid in a DAD2 "empty" structure (i.e. the DAD2/tolfenamic acid crystal structure in which tolfenamic acid had been removed) almost perfectly matched the pose observed for this compound in the crystal structure, with a docking score of –10.6 kcal/mol (35). Using the same methodology we docked five commercially available QADD/QADs (**0, 5–8**, Figure 1c) and three proposed synthetic QADD (**2–4**, Figure 1c) in DAD2's binding cavity. In all cases, the docking pose of the docked compound superimposed well with tolfenamic acid (Supplementary Figure S1). The

corresponding docking scores ranged from –12.0 to –9.8 kcal/mol, suggesting that these compounds have a similar potential, if not better, to inhibit DAD2 than tolfenamic acid (Table 2).

Chemical syntheses

QADD **0** and QAD **5–8** are commercially available (Experimental section). QADDs **2–4** were synthesized using an adapted literature procedure (52). The intermediate ureas were accessed through the treatment of 2-bromobenzamide with oxalyl chloride and the appropriate aniline (Supplementary Experimental section). The respective ureas were then dissolved in dry DMF and treated with freshly sublimed potassium *tert*-butoxide to afford the corresponding QADD, via an intramolecular nucleophilic substitution reaction (Figure 1d) (52). The reaction proceeded smoothly to afford QADD **3** and **4**. However, under these reaction conditions, the intramolecular cyclisation of the urea precursor of QADD **1** gave an unexpected hydroxylation *ortho* to the nitro group to provide QADD **2** in low yield. The same molecule was subsequently made in higher yield by starting with 4-hydroxy-3-nitroaniline. QADD **2** was co-crystallized with DAD2 (see below) and the 1.63 Å resolution crystal structure confirmed the hydroxylated structure. Whilst the mechanism of hydroxylation is unknown, there is a precedent for aromatic hydroxylation *ortho* to a nitro group, suspected to involve radical peroxide (53).

Binding and kinetics assays

To experimentally assess binding of QADs and QADDs to SL receptors, we tested whether QADD **0**, **2–8** were able to trigger stabilization of DAD2, AtD14 and OsD14 in a DSF assay. Using this assay, we previously showed that the thermal stability of the petunia, *Arabidopsis*, and rice SL receptors (DAD2, AtD14 and OsD14, respectively) is strongly

increased upon binding of inhibitors inside their internal cavity (35). In a SAR study of 138 compounds closely related to tolfenamic acid, we further found that one compound, 2-(2'-methyl-3'-nitroanilino)benzoic acid (MNAB), triggered the strongest stabilization of all three receptors, with melting temperature shifts of +7.0, +4.4 and +3.5°C being observed for DAD2, AtD14 and OsD14, respectively, thereby providing a benchmark for the evaluation of the new QADDs **0**, **2–8** (35). As seen in Figure 2a only QADD **2** triggered a stabilization of DAD2 although the thermal shift (ΔTm = +4.8°C) was lower than for MNAB. QADD **2** also stabilized AtD14 (ΔTm = +3.9°C, Figure 2b) but did not trigger thermal stabilization of OsD14 (ΔTm = –0.4°C, Figure 2c). In contrast to the *in silico* docking study that predicted all QAD/QADDs to efficaciously bind to DAD2, the other compounds showed no or only a small stabilizing effect on all three proteins (ΔTm < 1.6°C, Figure 2a-c). To confirm the DSF results, we measured the K_d values of QADD **2** to DAD2, AtD14 and OsD14 using intrinsic fluorescence (Figure 3a-c). K_d values of QADD **2** to DAD2 and AtD14 were 18.8 ± 1.8 (Fig 3a) and 19.2 ± 0.7 µM (Fig 3b), respectively, which represent ~4x and ~2x increases compared with the K_d values of MNAB to these two proteins (35). In agreement with the DSF assay, the binding of QADD **2** to OsD14 was much weaker and the K_d value could not be determined accurately (K_d = 276 ± 119 µM, Fig 3c). Taken together, the DSF and intrinsic fluorescence assays showed that QADD **2** successfully binds to both DAD2 and AtD14, albeit with reduced affinity compared to MNAB; however, binding of QADD **2** to OsD14 is very weak. Pre-steady state inhibition kinetics using YLG, a profluorescent probe that releases fluorescein upon hydrolysis by SL receptors (13), have previously been used to estimate apparent K_i values of MNAB for DAD2, AtD14 and OsD14 (K_i = 0.16, 1.9 and 2.4 µM, respectively, (35)). Using the same setup, the apparent K_i of QADD **2** for DAD2 and AtD14 were 1.03 ± 0.06 and 4.33 ±

291 0.32 µM, respectively, (Figure 3d-e) again showing that QADD **2** is less potent in inhibiting SL
292 receptors *in vitro* than MNAB.

293 We further showed that QADD **2** inhibits the GR24-dependent interaction between DAD2
294 and the downstream SL-signalling targets PhMAX2A and PhD53A using yeast two-hybrid
295 assays (Figure 4). However, in both cases, QADD **2** was ~10x less effective than tolfenamic
296 acid in these assays (35).

297 Crystal structure of DAD2 in complex with QADD 2

298 Tolfenamic acid-related compounds inhibit strigolactone receptors by binding inside their
299 internal cavities through a combination of hydrophobic interactions with the side chains of
300 four Phe residues lining the interior of the cavity (Phe27, Phe125, Phe158, Phe194; all
301 residue numbers refer to the DAD2 sequence) and electrostatic interactions with Ser96 and
302 His246 from the catalytic triad, and with Ser219 from the activation loop (35). Furthermore,
303 the relative positions of the side chain of His 246 and of the carboxylic group of tolfenamic
304 acid-related compounds suggested that His 246 could be protonated to form a salt bridge
305 anchoring the bound compound inside the cavity (35). To understand the discrepancies
306 between the *in silico* docking studies and the experimental results, we co-crystallized DAD2
307 with QADD **2** and solved its structure to 1.63 Å resolution (Table 1). Excellent electron
308 density was observed for QADD **2** inside DAD2's internal cavity (Figure 5) allowing detailed
309 comparisons with the binding mode of MNAB, its closest parent compound (Figure 1). As
310 seen in Figure 5, QADD **2** binds inside DAD2's cavity in a conformation totally different from
311 that of MNAB: instead of having rings X and Y of both compounds superimposed, as
312 predicted by the docking study, QADD **2** binds in a "back-to-front" conformation where the
313 X ring roughly occupies the position of the Y ring of MNAB while the Y ring sits well above

314 the X ring of MNAB and is rotated by ~90° compared to the X ring of MNAB (Figure 6a).
315 Consequently, while the docking study predicted that one of the carbonyl groups of the Z
316 ring would interact with Ser96, it is in fact the serendipitous hydroxyl group on the Y ring
317 that anchors QADD **2** to Ser96, while additional interactions occur between the nitro group
318 of QADD **2**, positioned deep inside the cavity, and the catalytic residues Ser96 and His246. In
319 addition, one of the carbonyl groups on the Z ring forms a hydrogen bond with the hydroxyl
320 group of Ser219 to stabilize the activation loop, thereby replacing the interaction previously
321 seen between this residue and the carboxylic group of MNAB (Figure 6a). Despite the large
322 differences observed between the binding mode and conformations of two compounds,
323 only relatively small movements are observed for the protein residues lining DAD2's internal
324 cavity (Figure 6a). Among these, rotations of the side chains of Phe125, Phe158 and Phe194
325 are observed to optimize interactions with rings Y and Z of QADD **2**, and the side chain of
326 Val193 is displaced by almost 2 Å to occupy some of the space previously filled by the X ring
327 of MNAB (Figure 6a, Supplementary Figure S2). In contrast, the position of the side chain of
328 Phe27, which was previously found to form an essential hydrophobic stacking interaction
329 with the X ring MNAB (35) but now has only weak hydrophobic contacts with rings X and Y
330 of QADD **2**, remains unchanged. Likewise, the side chain of His 218 has the same
331 conformation as in the MNAB-bound structure, although this residue now has no direct
332 contact with QADD **2** (Figure 6a). We next compared the binding site of QADD **2** with that of
333 GR24 observed in the rice OsD14 structure (28). As seen on Figure 6b, the two compounds
334 overlap at the same position within the internal cavity, confirming that QADD **2** acts as a
335 competitive inhibitor to prevent access to the active site cavity to the SL compound.

Revisiting the docking study

The unexpected binding mode of QADD **2** inside DAD2's cavity prompted us to revisit the results of the docking study. To this end, the nine different docking poses obtained for QADD **2** in the DAD2/tolfenamic acid empty crystal structure (ranked in increasing order of their calculated binding affinity) were compared with the experimentally determined poses of both tolfenamic acid and of QADD **2** inside DAD2's cavity observed in the respective crystal structures (Supplementary Tables 2A and 2B). Among these, docking poses #1 and, to a lesser extent, #5 have their ring structure superimposing well with tolfenamic acid and differ by a 180° rotation of their Y ring carrying the nitro group. Conversely, poses #4 and #6 share similarity with the conformation of QADD **2** seen in the crystal structure. Pose #6 in particular shows a reasonably good agreement with the crystal structure, while pose #4 has its Y ring rotated almost 180° compared with the structure, therefore presenting the nitro group in the wrong direction.

To complement these results, we next performed the same docking experiment but using the empty DAD2/QADD **2** crystal structure as the receptor. As described earlier, only relatively small conformational differences are observed for a few residues lining DAD2's internal cavity when QADD **2** is bound instead of tolfenamic acid. However, these are sufficient to drive the docking results toward the correct solution, with docking pose #1 of QADD **2** now matching almost perfectly the conformation seen in the structure (Supplementary Table 2B). In addition, docking pose #3 is also very close to the conformation observed in the crystal structure, with only the Y ring differing by a 180° rotation. In contrast to the previous docking study, none of the docking poses obtained using the DAD2/QADD **2** empty structure as receptor resemble the conformation seen for

359 tolfenamic acid. This is most likely because of the position of Val193 in the DAD2/QADD **2**
360 crystal structure that occupies some of the space previously filled by the X ring of tolfenamic
361 acid (Figure 5). Overall, these results confirm that, while docking can provide very valuable
362 insights into the binding mode of small molecular compounds inside protein binding
363 pockets, it is also extremely sensitive to the local environment of the receptor. In the
364 present case, the small conformational changes observed for a few of the residues lining the
365 internal cavity of DAD2 upon binding QADD **2** could not have been anticipated or
366 appropriately modelled to allow the initial docking study to accurately predict the back-to-
367 front binding mode of QADD **2** inside the cavity. Although poses showing similarities to the
368 true conformation of QADD **2** inside DAD2's cavity were present within the list of docking
369 solutions (at #6 and, to a lesser extent, at #4), the top solution mimicking the conformation
370 of tolfenamic acid/MNAB was the most plausible one given the knowledge available at the
371 time the study was done.

372 Among all QADs/QADDs tested in this study, only QADD **2** harbors the hydroxyl group on the
373 Y ring that directly interacts with the catalytic serine of the SL receptor at the bottom of the
374 cavity, and none of the other QADs/QADDs were able to bind to the receptor. This confirms
375 that anchoring of the compound through electrostatic interactions with the few polar
376 residues present inside the binding cavity is essential for a successful interaction. A
377 fundamental difference between *N*-phenylanthranilic acid derivatives and QAD/QADDs is
378 the presence of a negatively charged carboxylic group in *N*-phenylanthranilic acid
379 derivatives. In the crystal structure of DAD2 bound to tolfenamic acid, it was noted that the
380 respective positions of the carboxylic group of tolfenamic acid and of the side chain of
381 His246 from the catalytic triad suggested His246 to be protonated, thereby forming a salt
382 bridge with the carboxylic group of the bound compound (35). In contrast, the

electronegative nitro group of QADD **2** does not point directly towards His246 but sits on the side and is further away. Furthermore, the lack of binding observed for QAD/QADD **6** and **9** (both carrying a similar nitro group at the same position, but lacking the addition hydroxyl group that interacts with Ser96) suggests that despite the electronegative character of the oxygen atoms, the presence of the nitro group is not sufficient to trigger a stable interaction with DAD2, and that interactions between the compound and both Ser96 and His246 are required for successful binding. Altogether, the lack of binding of most of the QADs/QADDs tested here and the lower binding affinity observed for QADD **2** indirectly support the hypothesis that a salt bridge between the carboxylic group of *N*-phenylanthranilic acid derivatives and the catalytic histidine of DAD2 deep inside the internal cavity is a key driver for the high affinity observed between DAD2 and this class of compounds.

In planta activity of QADD 2

In planta activity of QADD **2** was tested in *Arabidopsis* bud assays and compared with tolfenamic acid whose activity has been described previously (35). As seen in Figure 7, QADD **2** showed effects on bud growth similar to tolfenamic acid, both in presence and absence of GR24. We noted previously that the relatively high concentration of tolfenamic acid required to give a physiological response in plants contrasts with the potency observed for this compound *in vitro*, and suggested that uptake and/or transport of tolfenamic acid may be limiting factors for its activity *in planta* (35). Indeed, intrinsic characteristics of tolfenamic acid suggest some potential drawbacks for *in planta* applications: a very low solubility in aqueous media and the presence of a charged group that may affect passive transport into plants. In contrast, we observe here that QADD **2,** while less potent than

406 tolfenamic acid *in vitro*, shows similar levels of activity when tested on bud growth. QADD **2**
407 may therefore compensate a lower potency for the SL receptor by increased levels of
408 solubility, uptake and/or transport *in planta*, suggesting a fine balance between potency and
409 bioavailability of candidate compounds to obtain successful plant growth regulators
410 targeting the strigolactone pathway. A firm conclusion on the relative efficacy of these two
411 compounds will, however, require additional analyses. While further studies will also be
412 required to fully understand the effects of different inhibitors on SL-regulated plant
413 responses at both genetic and physiological levels, our results establish QADD **2** as a novel
414 lead compound towards the generation of antagonists targeting plant SL receptors with
415 improved potency and bioavailability.

Data Availability

The crystal structure of DAD2 in complex with 1-(3-nitro-4-hydroxyphenyl)-1H-quinazoline-2,4-dione (**2**) has been deposited in the Protein Data Bank, with entry code 6O5J.

Acknowledgments

We thank William A. Denny from the Auckland Cancer Society for his analysis of our SAR study and initial suggestion of investigating QAD/QADDs, Revel S.M. Drummond for advice with the yeast two-hybrid experiments and members of the Laboratory of Structural Biology (University of Auckland) for help with X-ray data collection. This research was undertaken on the MX1 beamline at the Australian Synchrotron, part of ANSTO.

Declaration of interest

The authors declare no competing financial interest.

Funding information

This work was supported by funding from Plant and Food Research and a Marsden grant from the Royal Society Te Apārangi (contract PAF1301).

Author Contributions

CH, HWL, PS, ZL and KCS performed experiments. LL, BCH and NBP synthesized the QADDs. CH wrote the manuscript with input from all authors. CH and KCS conceived and supervised the project.

References

1. Gomez-Roldan V, Fermas S, Brewer PB, Puech-Pages V, Dun EA, Pillot J-P, et al. Strigolactone inhibition of shoot branching. Nature. 2008;455(7210):189-94.

2. Kapulnik Y, Delaux PM, Resnick N, Mayzlish-Gati E, Wininger S, Bhattacharya C, et al. Strigolactones affect lateral root formation and root-hair elongation in *Arabidopsis*. Planta. 2011;233(1):209-16.

3. Pandey A, Sharma M, Pandey GK. Emerging roles of strigolactones in plant responses to stress and development. Front Plant Sci. 2016;7:434.

4. Rasmussen A, Mason MG, De Cuyper C, Brewer PB, Herold S, Agusti J, et al. Strigolactones suppress adventitious rooting in *Arabidopsis* and pea. Plant Physiol. 2012;158(4):1976-87.

5. Snowden K, Simkin A, Janssen B, Templeton K, Loucas H, Simons J, et al. The *decreased apical dominance1*/*Petunia hybrida CAROTENOID CLEAVAGE DIOXYGENASE8* gene affects branch production and plays a role in leaf senescence, root growth, and flower development. Plant Cell. 2005;17(3):746-59.

6. Umehara M, Hanada A, Yoshida S, Akiyama K, Arite T, Takeda-Kamiya N, et al. Inhibition of shoot branching by new terpenoid plant hormones. Nature. 2008;455(7210):195-200.

7. Woo HR, Chung KM, Park J-H, Oh SA, Ahn T, Hong SH, et al. ORE9, an F-Box protein that regulates leaf senescence in *Arabidopsis*. Plant Cell. 2001;13(8):1779-90.

8. Yamada Y, Furusawa S, Nagasaka S, Shimomura K, Yamaguchi S, Umehara M. Strigolactone signaling regulates rice leaf senescence in response to a phosphate deficiency. Planta. 2014;240(2):399-408.

9. Akiyama K, Matsuzaki K, Hayashi H. Plant sesquiterpenes induce hyphal branching in arbuscular mycorrhizal fungi. Nature. 2005;435(7043):824-7.

10. Al-Babili S, Bouwmeester HJ. Strigolactones, a novel carotenoid-derived plant hormone. Annu Rev Plant Biol. 2015;66:161-86.

11. Brewer PB, Koltai H, Beveridge CA. Diverse roles of strigolactones in plant development. Molecular Plant. 2013;6(1):18-28.

12. Khosla A, Nelson DC. Strigolactones, super hormones in the fight against *Striga*. Curr Opin Plant Biol. 2016;33:57-63.

13. Tsuchiya Y, Yoshimura M, Sato Y, Kuwata K, Toh S, Holbrook-Smith D, et al. PARASITIC PLANTS. Probing strigolactone receptors in *Striga* hermonthica with fluorescence. Science. 2015;349(6250):864-8.

14. Lumba S, Holbrook-Smith D, McCourt P. The perception of strigolactones in vascular plants. Nat Chem Biol. 2017;13(6):599-606.

15. de Saint Germain A, Clave G, Badet-Denisot MA, Pillot JP, Cornu D, Le Caer JP, et al. An histidine covalent receptor and butenolide complex mediates strigolactone perception. Nat Chem Biol. 2016;12(10):787-94.

16. Hamiaux C, Drummond RS, Janssen BJ, Ledger SE, Cooney JM, Newcomb RD, et al. DAD2 is an α/β hydrolase likely to be involved in the perception of the plant branching hormone, strigolactone. Curr Biol. 2012;22(21):2032-6.

17. Jiang L, Liu X, Xiong G, Liu H, Chen F, Wang L, et al. DWARF 53 acts as a repressor of strigolactone signalling in rice. Nature. 2013;504(7480):401-5.

18. Yao R, Ming Z, Yan L, Li S, Wang F, Ma S, et al. DWARF14 is a non-canonical hormone receptor for strigolactone. Nature. 2016;536(7617):469-73.

19. Zhao LH, Zhou XE, Wu ZS, Yi W, Xu Y, Li S, et al. Crystal structures of two phytohormone signal-transducing α/β hydrolases: karrikin-signaling KAI2 and strigolactone-signaling DWARF14. Cell Res. 2013;23(3):436-9.

20. Stanga JP, Morffy N, Nelson DC. Functional redundancy in the control of seedling growth by the karrikin signaling pathway. Planta. 2016;243(6):1397-406.

21. Zhou F, Lin Q, Zhu L, Ren Y, Zhou K, Shabek N, et al. D14-SCF(D3)-dependent degradation of D53 regulates strigolactone signalling. Nature. 2013;504(7480):406-10.

22. Bythell-Douglas R, Waters MT, Scaffidi A, Flematti GR, Smith SM, Bond CS. The structure of the karrikin-insensitive protein (KAI2) in *Arabidopsis thaliana*. PLoS ONE. 2013;8(1):e54758.

23. Guo Y, Zheng Z, La Clair JJ, Chory J, Noel JP. Smoke-derived karrikin perception by the α/β-hydrolase KAI2 from *Arabidopsis*. Proc Natl Acad Sci USA. 2013;110(20):8284-9.

24. Kagiyama M, Hirano Y, Mori T, Kim SY, Kyozuka J, Seto Y, et al. Structures of D14 and D14L in the strigolactone and karrikin signaling pathways. Genes Cells. 2013;18(2):147-60.

25. Nakamura H, Xue YL, Miyakawa T, Hou F, Qin HM, Fukui K, et al. Molecular mechanism of strigolactone perception by DWARF14. Nat Commun. 2013;4:2613.

26. Toh S, Holbrook-Smith D, Stogios PJ, Onopriyenko O, Lumba S, Tsuchiya Y, et al. Structure-function analysis identifies highly sensitive strigolactone receptors in *Striga*. Science. 2015;350(6257):203-7.

27. Xu Y, Miyakawa T, Nakamura H, Nakamura A, Imamura Y, Asami T, et al. Structural basis of unique ligand specificity of KAI2-like protein from parasitic weed *Striga hermonthica*. Sci Rep. 2016;6:31386.

28. Zhao LH, Zhou XE, Yi W, Wu Z, Liu Y, Kang Y, et al. Destabilization of strigolactone receptor DWARF14 by binding of ligand and E3-ligase signaling effector DWARF3. Cell Res. 2015;25(11):1219-36.

506 29. Nakamura H, Asami T. Target sites for chemical regulation of strigolactone signaling.
507 Front Plant Sci. 2014;5:623.

508 30. Waters MT. Spoilt for choice: new options for inhibitors of strigolactone signaling.
509 Mol Plant. 2019;12(1):21-3.

510 31. Holbrook-Smith D, Toh S, Tsuchiya Y, McCourt P. Small-molecule antagonists of
511 germination of the parasitic plant *Striga hermonthica*. Nat Chem Biol. 2016;12(9):724-9.

512 32. Mashita O, Koishihara H, Fukui K, Nakamura H, Asami T. Discovery and identification
513 of 2-methoxy-1-naphthaldehyde as a novel strigolactone-signaling inhibitor. J Pestic Sci.
514 2016;41(3):71-8.

515 33. Xiang H, Yao R, Quan T, Wang F, Chen L, Du X, et al. Simple beta-lactones are potent
516 irreversible antagonists for strigolactone receptors. Cell Res. 2017;27(12):1525-8.

517 34. Yoshimura M, Sato A, Kuwata K, Inukai Y, Kinoshita T, Itami K, et al. Discovery of
518 shoot branching regulator targeting strigolactone receptor DWARF14. ACS Cent Sci.
519 2018;4(2):230-4.

520 35. Hamiaux C, Drummond RSM, Luo Z, Lee HW, Sharma P, Janssen BJ, et al. Inhibition of
521 strigolactone receptors by *N*-phenylanthranilic acid derivatives: Structural and functional
522 insights. J Biol Chem. 2018;293(17):6530-43.

523 36. Shahul Hameed U, Haider I, Jamil M, Kountche BA, Guo X, Zarban RA, et al. Structural
524 basis for specific inhibition of the highly sensitive ShHTL7 receptor. EMBO Rep.
525 2018;19(9):e45619.

526 37. Takeuchi J, Jiang K, Hirabayashi K, Imamura Y, Wu Y, Xu Y, et al. Rationally designed
527 strigolactone analogs as antagonists of the D14 receptor. Plant Cell Physiol.
528 2018;59(8):1545-54.

529 38. Nakamura H, Hirabayashi K, Miyakawa T, Kikuzato K, Hu W, Xu Y, et al. Triazole ureas
530 covalently bind to strigolactone receptor and antagonize strigolactone responses. Mol Plant.
531 2019;12(1):44-58.

532 39. Battye TG, Kontogiannis L, Johnson O, Powell HR, Leslie AG. iMOSFLM: a new
533 graphical interface for diffraction-image processing with MOSFLM. Acta Crystallogr D Biol
534 Crystallogr. 2011;67(Pt 4):271-81.

535 40. Evans PR, Murshudov GN. How good are my data and what is the resolution? Acta
536 Crystallogr D Biol Crystallogr. 2013;69(Pt 7):1204-14.

537 41. Winn MD, Ballard CC, Cowtan KD, Dodson EJ, Emsley P, Evans PR, et al. Overview of
538 the CCP4 suite and current developments. Acta Crystallogr D Biol Crystallogr. 2011;67(Pt
539 4):235-42.

540 42. McCoy AJ, Grosse-Kunstleve RW, Adams PD, Winn MD, Storoni LC, Read RJ. Phaser
541 crystallographic software. J Appl Crystallogr. 2007;40(Pt 4):658-74.

43. Murshudov GN, Skubak P, Lebedev AA, Pannu NS, Steiner RA, Nicholls RA, et al. REFMAC5 for the refinement of macromolecular crystal structures. Acta Crystallogr D Biol Crystallogr. 2011;67(Pt 4):355-67.

44. Emsley P, Lohkamp B, Scott WG, Cowtan K. Features and development of Coot. Acta Crystallogr D Biol Crystallogr. 2010;66(Pt 4):486-501.

45. Lebedev AA, Young P, Isupov MN, Moroz OV, Vagin AA, Murshudov GN. JLigand: a graphical tool for the CCP4 template-restraint library. Acta Crystallogr D Biol Crystallogr. 2012;68(Pt 4):431-40.

46. Joosten RP, Joosten K, Cohen SX, Vriend G, Perrakis A. Automatic rebuilding and optimization of crystallographic structures in the Protein Data Bank. Bioinformatics. 2011;27(24):3392-8.

47. O'Boyle NM, Banck M, James CA, Morley C, Vandermeersch T, Hutchison GR. Open Babel: An open chemical toolbox. J Cheminform. 2011;3:33.

48. Morris GM, Huey R, Lindstrom W, Sanner MF, Belew RK, Goodsell DS, et al. AutoDock4 and AutoDockTools4: Automated docking with selective receptor flexibility. J Comput Chem. 2009;30(16):2785-91.

49. Trott O, Olson AJ. AutoDock Vina: improving the speed and accuracy of docking with a new scoring function, efficient optimization, and multithreading. J Comput Chem. 2010;31(2):455-61.

50. James P, Halladay J, Craig EA. Genomic libraries and a host strain designed for highly efficient two-hybrid selection in yeast. Genetics. 1996;144(4):1425-36.

51. Maier R, Brandner C, Hintner H, Bauer J, Onder K. Construction of a reading frame-independent yeast two-hybrid vector system for site-specific recombinational cloning and protein interaction screening. BioTechniques. 2008;45(3):235-44.

52. Bowman WR, Heaney H, Smith PHG. Synthesis of 1H-quinazoline-4-ones using intramolecular aromatic nucleophilic substitution. Arkivoc. 2003:434-42.

53. Mattersteig G, Pritzkow W, Voerckel V. The reaction of organic hydroperoxides with aromatic nitro compounds: First examples of a Vicarious Nucleophilic Hydroxylation. J Prakt Chemie. 1990;332(4):569-72.

Tables

Table 1. Data collection and refinement statistics. Values in parentheses are for the last resolution shell.

Crystal	$DAD2_{C89Q}$ with QADD **2**
PDB entry code	6O5J
Space group	P1
Cell parameters (Å and °)	a=36.63, b=56.83, c=68.80 α=95.69, β=94.59, ɣ=108.74
Dataset	
λ (Å)	0.9537
Reflections observed	243,675
Unique reflections	62,194
Resolution range (Å)	31.3–1.63 (1.66–1.63)
R_{sym}	0.08 (0.6)
$CC_{1/2}$	0.998 (0.757)
I/σ(I)	11.8 (2.2)
Completeness	96.0 (94.6)
Multiplicity	3.9 (3.9)
B_{wilson} ($Å^2$)	9.7
Refinement	
Resolution (Å)	29.37–1.63 (1.67–1.63)
Reflections	59,313
Total number of atoms	4,842
TLS groups	2
R_{work}/R_{free}	14.4 / 18.2 (20.3 / 21.6)
RMSD bonds (Å) / angles (°)	0.0156 / 1.94
Average B factors ($Å^2$) (protein / water / inhibitor)	19.3 / 29.1 / 14.0
Ramachandran statistics of φ/ψ angles (%)	Most favored: 90.5 Additional favored: 9.1 Generously favored: 0.4 Disallowed: 0

576 **Table 2.** Docking scores of QADs/QADDs inside DAD2's binding cavity.

Compound #	Vina docking score (kcal/mol)
0	–11.2
2	–10.2
3	–11.5
4	–11.8
5	–9.8
6	–10.3
7	–12.0
8	–11.6

577

Figure Legends

Figure 1. Compound structures and synthetic scheme. (a) *N*-(2-methylphenyl)anthranilic acid, the core pharmacophore as identified by previous SAR study. (b) Schematic representation of ring closure hypothesis to maximize intra-molecular hydrogen bonding and minimize ring twist, leading to 1-phenylquinazoline-2,4(1H,3H)-dione (**0**) as novel reference compound. (c) **1–8**: QADD and QAD structures mentioned and used in this study; **9**: 2-(2'-methyl-3'-nitroanilino)benzoic acid (MNAB); **10**: tolfenamic acid. Ring labels used throughout the manuscript are shown in red. (d) Synthetic scheme of QADDs.

Figure 2. DSF assay of DAD2 (a), AtD14 (b) and OsD14 (c) in presence of QADs/QADDs. Top panels represent the experimental melting curves of each protein in presence of QAD/QADD **0**, **2–8** and in presence of DMSO. Bottom panels are the derivatives of the melting curve from which melting temperatures are determined by the position of the minimum. Dotted lines indicate the melting temperature of proteins in the presence of DMSO (grey line) and in the presence of the best compound (colored lines). Melting temperature shifts are calculated according to: ΔTm = Tm (compound) – Tm (DMSO).

Figure 3. QADD 2 binding and inhibition. (a), (b) and (c) Binding of QADD **2** to DAD2, AtD14 and OsD14, respectively, using intrinsic fluorescence**.** Each data point is the mean ± s.e.m. of three technical replicates. (d) and (e) YLG hydrolysis competition assays by QADD **2** for DAD2 and At14, respectively. Each data point is the mean ± s.e.m. of three technical replicates. For some data points, error bars are smaller than the symbol used for the data

and do not appear on the graphs. All individual replicates for each compound concentration were included during the non-linear global fit analysis using the competitive inhibition model.

Figure 4. Yeast two-hybrid analysis. Inhibition of (rac)-GR24-induced DAD2/PhMAX2A (a) and DAD2/PhD53A (b) interactions by QADD **2**. Protein-protein interactions are quantified by assaying β-galactosidase activity in a yeast two-hybrid liquid culture system. Each data point is the mean ± s.e.m. of three technical replicates.

Figure 5. Electron density map of bound QADD 2. The final sigmaA-weighted 2mFo-DFc electron density map contoured at 1.0 sigma around QADD **2** is shown in blue in two orientations (rotated ~90° along the horizontal axis). QADD **2** and the catalytic serine (Ser 96) are drawn in stick mode.

Figure 6. QADD 2 acts as a competitive inhibitor (a) Comparison of the binding modes of QADD **2** and MNAB inside DAD2's internal cavity. The DAD2/QADD **2** structure is drawn in green, while the DAD2/MNAB structure is drawn in pink. Hydrogen bonds are shown as dotted lines. (b) Comparison of the binding modes of QADD **2** and GR24 inside DAD2's internal cavity. The OsD14/GR24 structure (PDB 5DJ5, drawn in orange) was superimposed to the DAD2/QADD **2** structure in the same orientation as Figure 5a. OsD14 residues are labelled. QADD **2** (green) and GR24 (orange) are drawn in stick mode.

Figure 7. *In planta* activity of QADD 2, compared with tolfenamic acid. *Arabidopsis* bud growth assay, treated with 0.5 µM GR24 and/or 5 µM compound (tolfenamic acid and QADD **2**). Bud growth was normalized relative to the mock treated control. The violin plots show the median (solid line) and quartiles values (dotted lines), and the area of each plot represents the frequency distribution of the data, n=16. Statistical tests of differences between treatments were calculated by ANOVA and Fisher's protected LSD multiple comparisons test. Different letters indicate statistically significant results at $p < 0.05$. Data from the control and tolfenamic acid treated buds have been published previously (35), all data were collected at the same time.

a

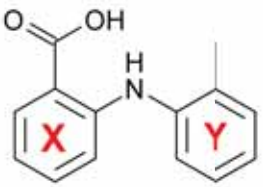

b

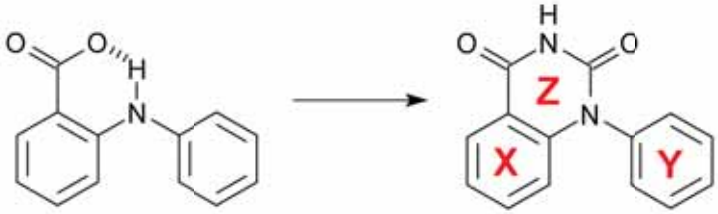

0

c

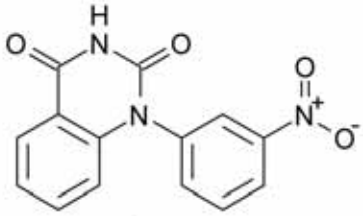

1

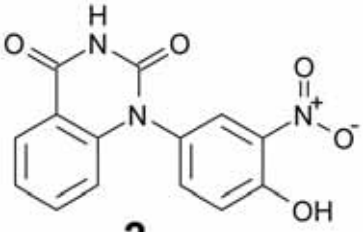

2

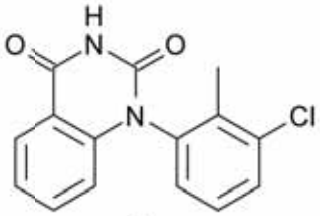

3

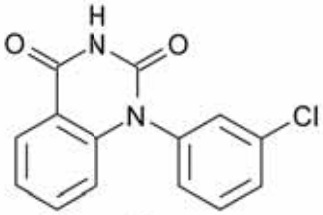

4

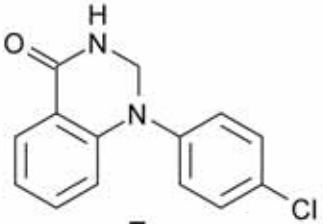

5

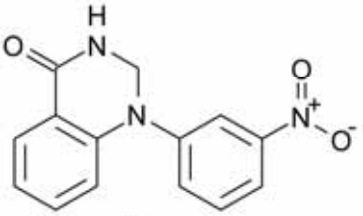

6

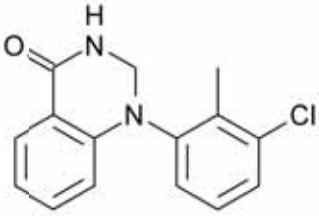

7

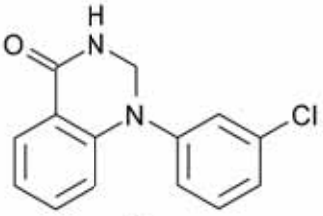

8

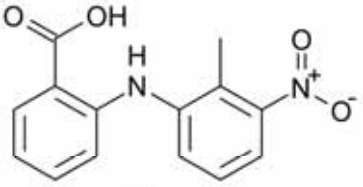

9

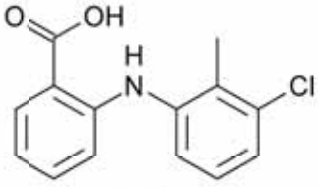

10

d

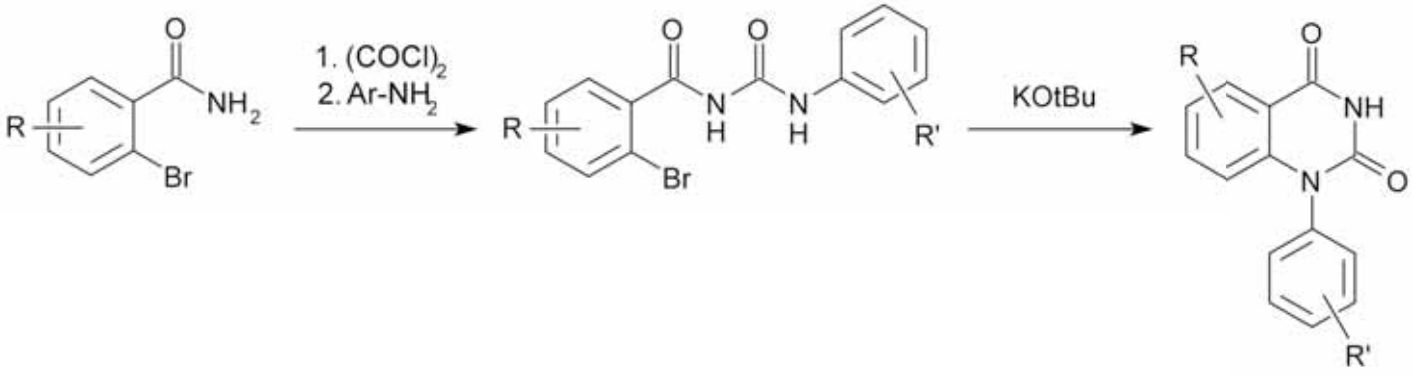

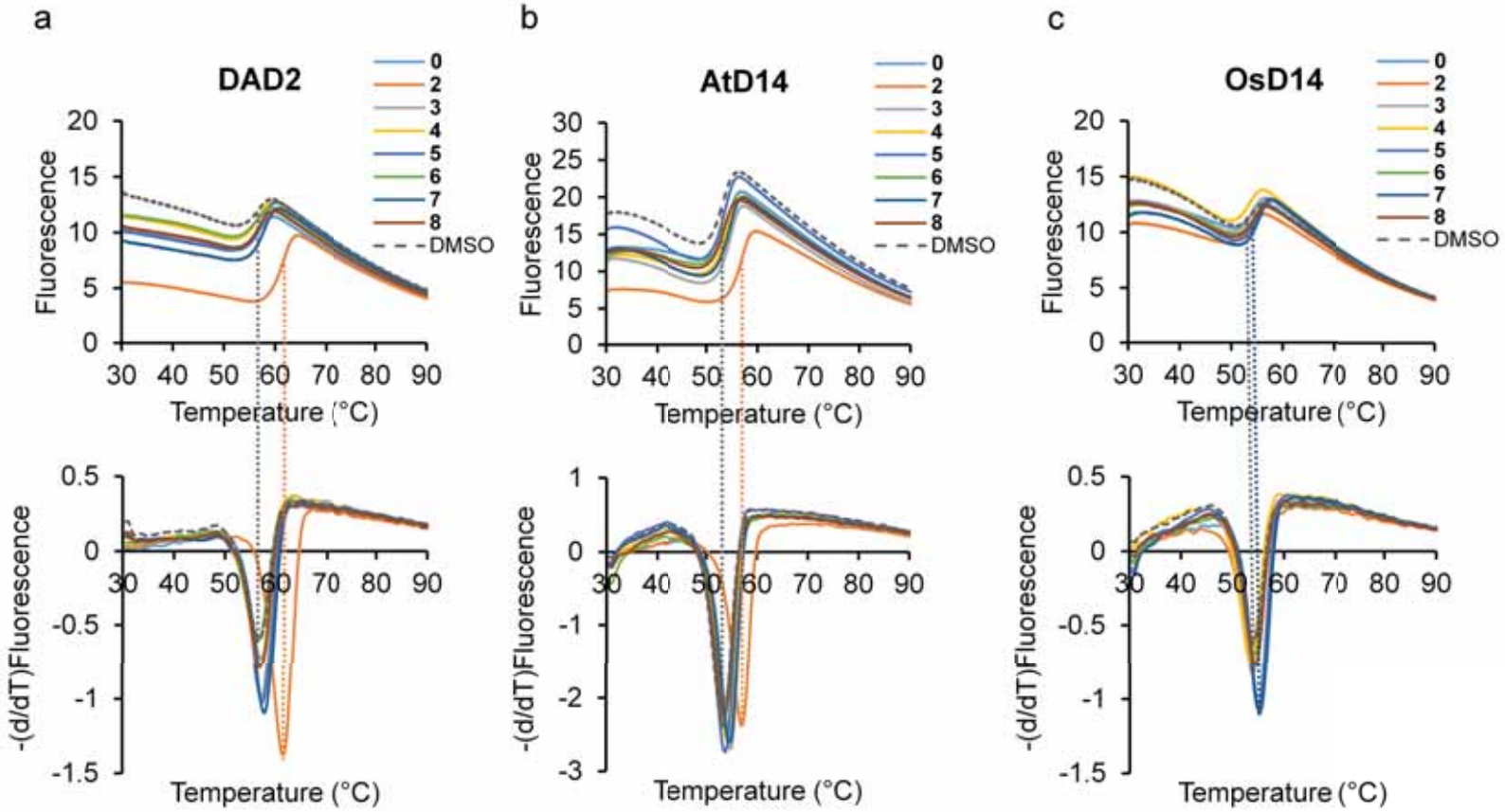
a
DAD2
0
2
3
4
5
6
7
8
DMSO
Fluorescence
Temperature (°C)
-(d/dT)Fluorescence
Temperature (°C)
b
AtD14
0
2
3
4
5
6
7
8
DMSO
Fluorescence
Temperature (°C)
-(d/dT)Fluorescence
Temperature (°C)
c
OsD14
0
2
3
4
5
6
7
8
DMSO
Fluorescence
Temperature (°C)
-(d/dT)Fluorescence
Temperature (°C)

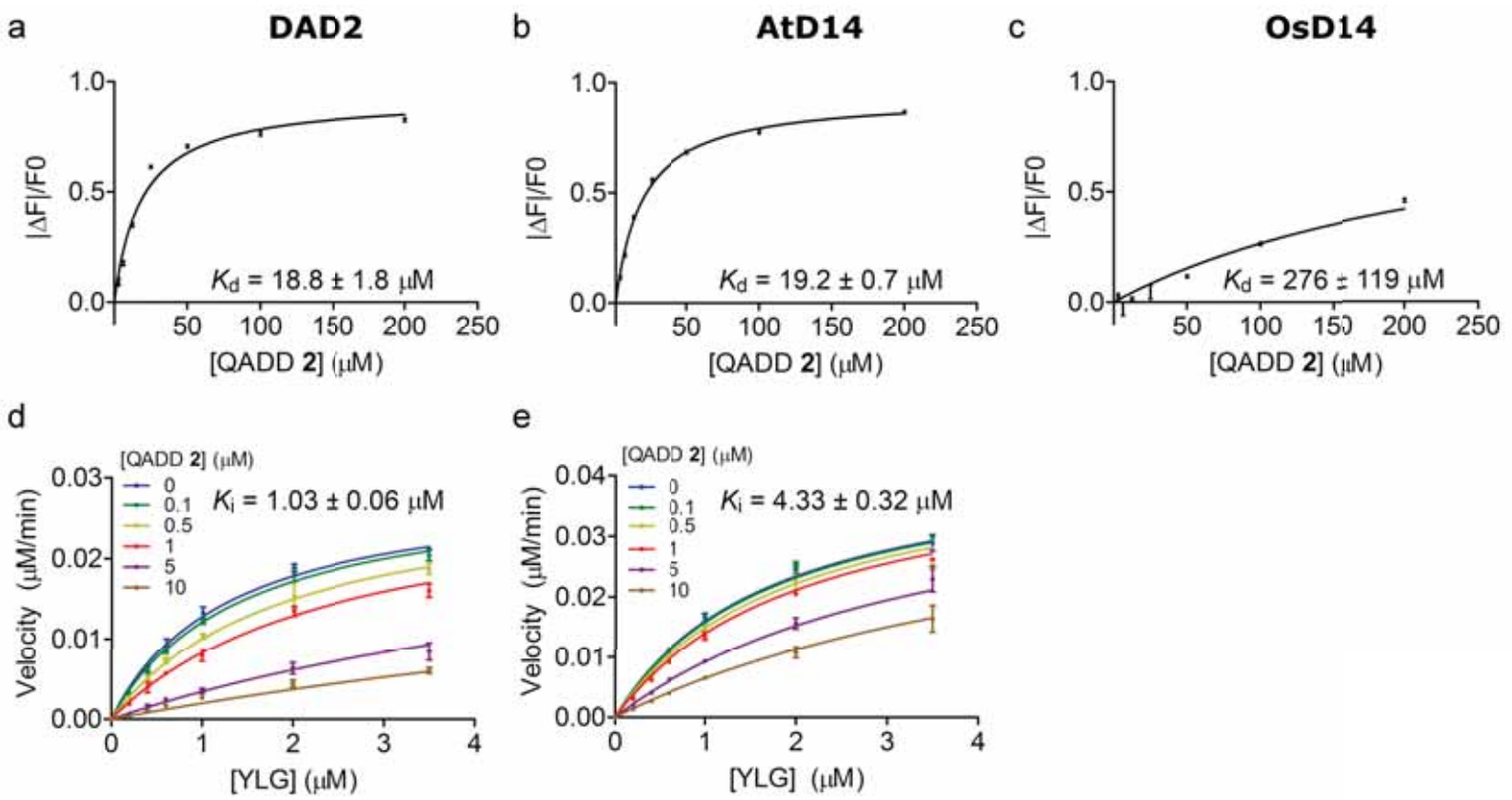
a
DAD2
b
AtD14
c
OsD14
|ΔF|/F0
1.0
0.5
0.0
50
100
150
200
250
[QADD 2] (μM)
K_d = 18.8 ± 1.8 μM
K_d = 19.2 ± 0.7 μM
K_d = 276 ± 119 μM
d
e
[QADD 2] (μM)
0
0.1
0.5
1
5
10
K_i = 1.03 ± 0.06 μM
K_i = 4.33 ± 0.32 μM
Velocity (μM/min)
0.03
0.02
0.01
0.00
0.04
0
1
2
3
4
[YLG] (μM)

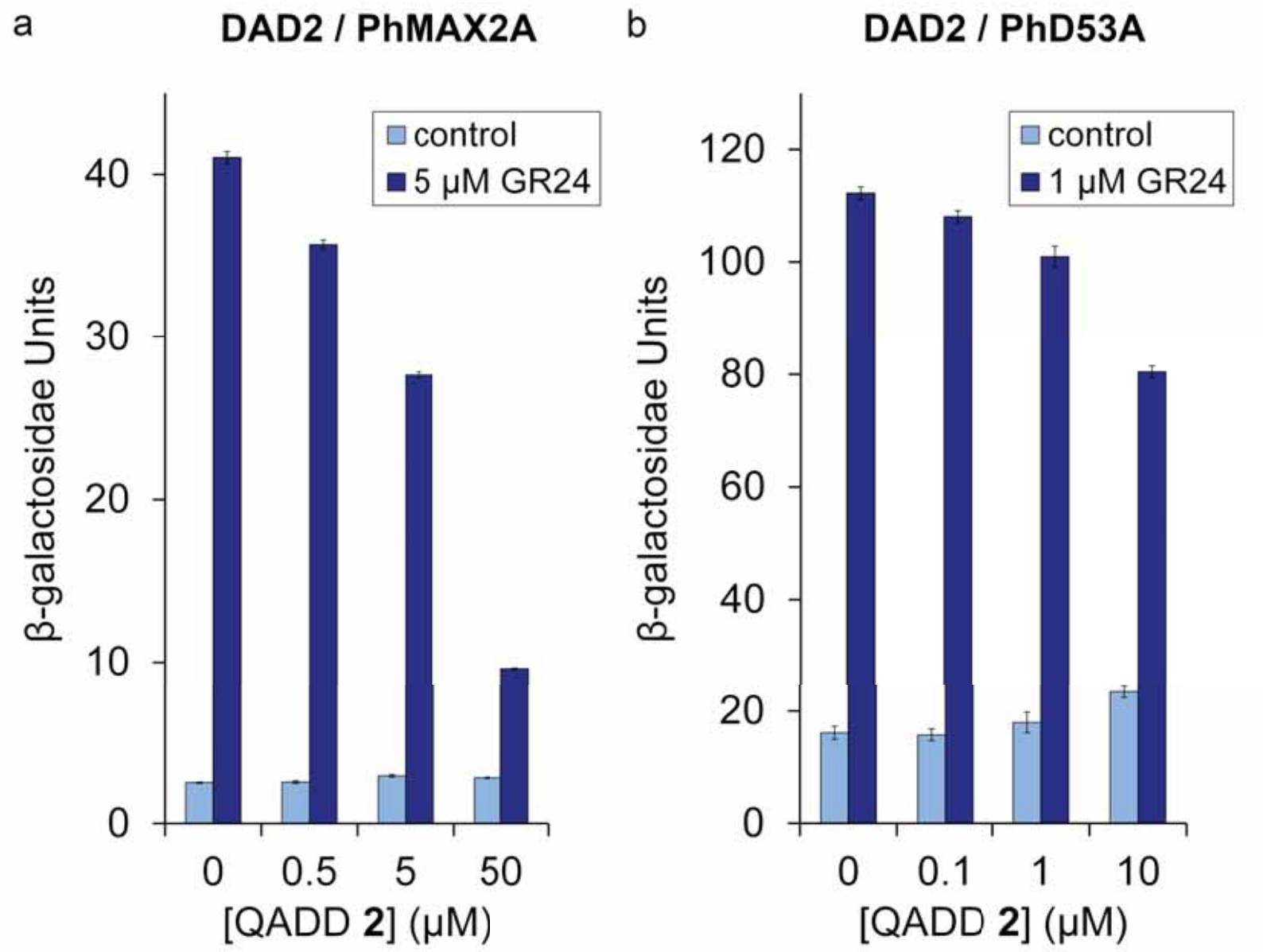
a
DAD2 / PhMAX2A
control
5 µM GR24
β-galactosidae Units
0
10
20
30
40
0
0.5
5
50
[QADD 2] (µM)
b
DAD2 / PhD53A
control
1 µM GR24
β-galactosidae Units
0
20
40
60
80
100
120
0
0.1
1
10
[QADD 2] (µM)

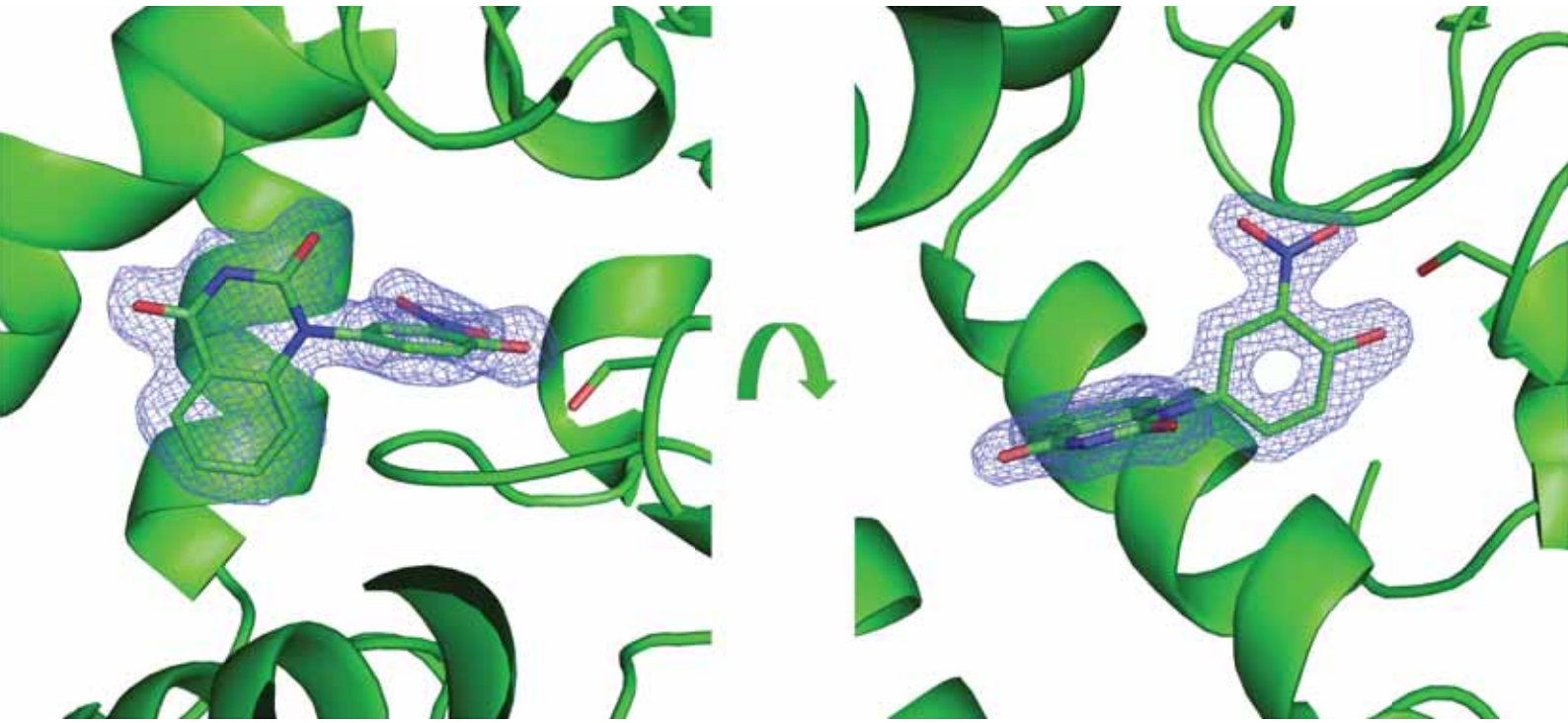

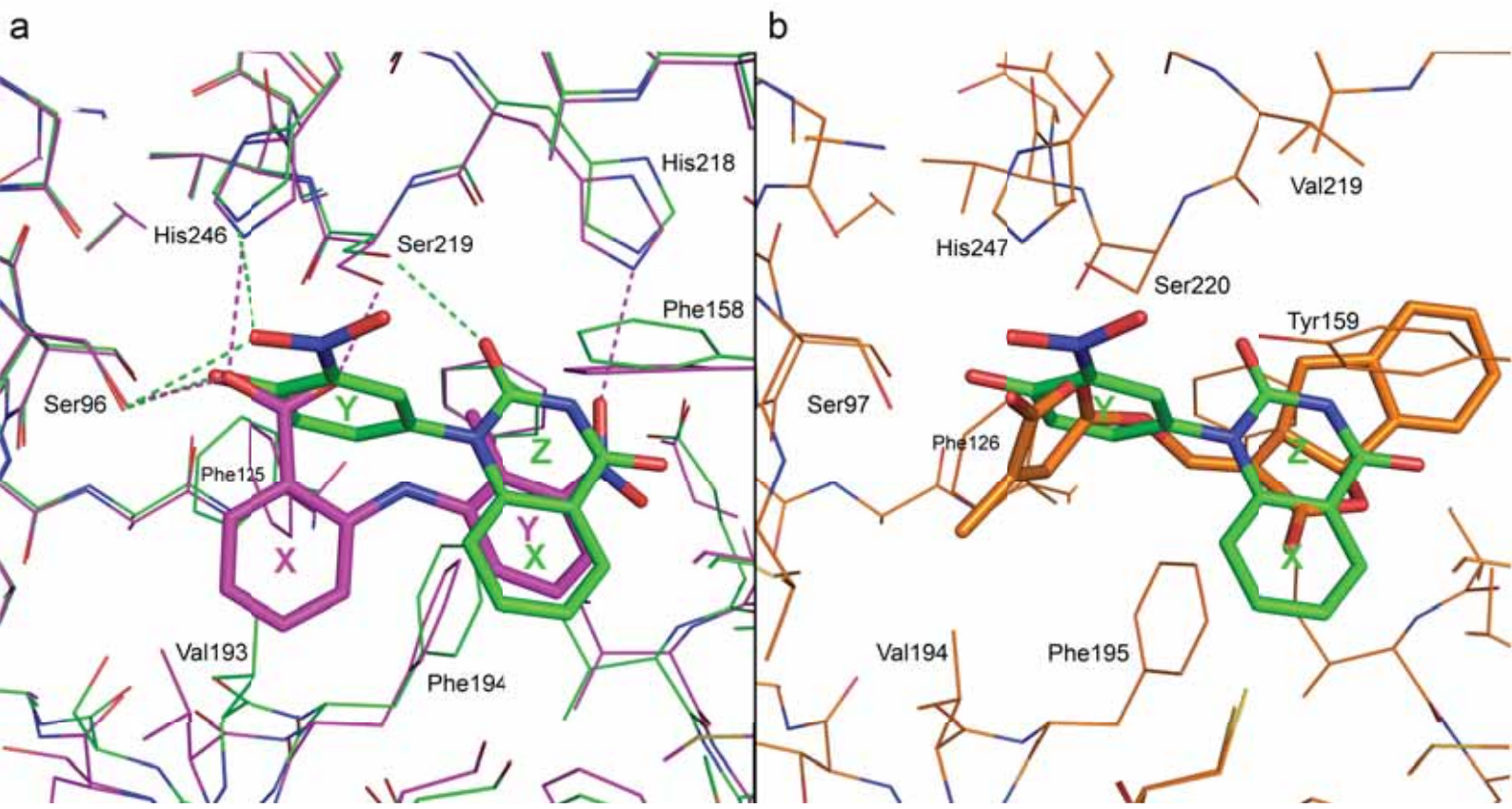
a
His246
Ser219
His218
Phe158
Ser96
Y
Z
Phe125
X
Y
X
Val193
Phe194
b
Val219
His247
Ser220
Tyr159
Ser97
Y
Phe126
Z
X
Val194
Phe195

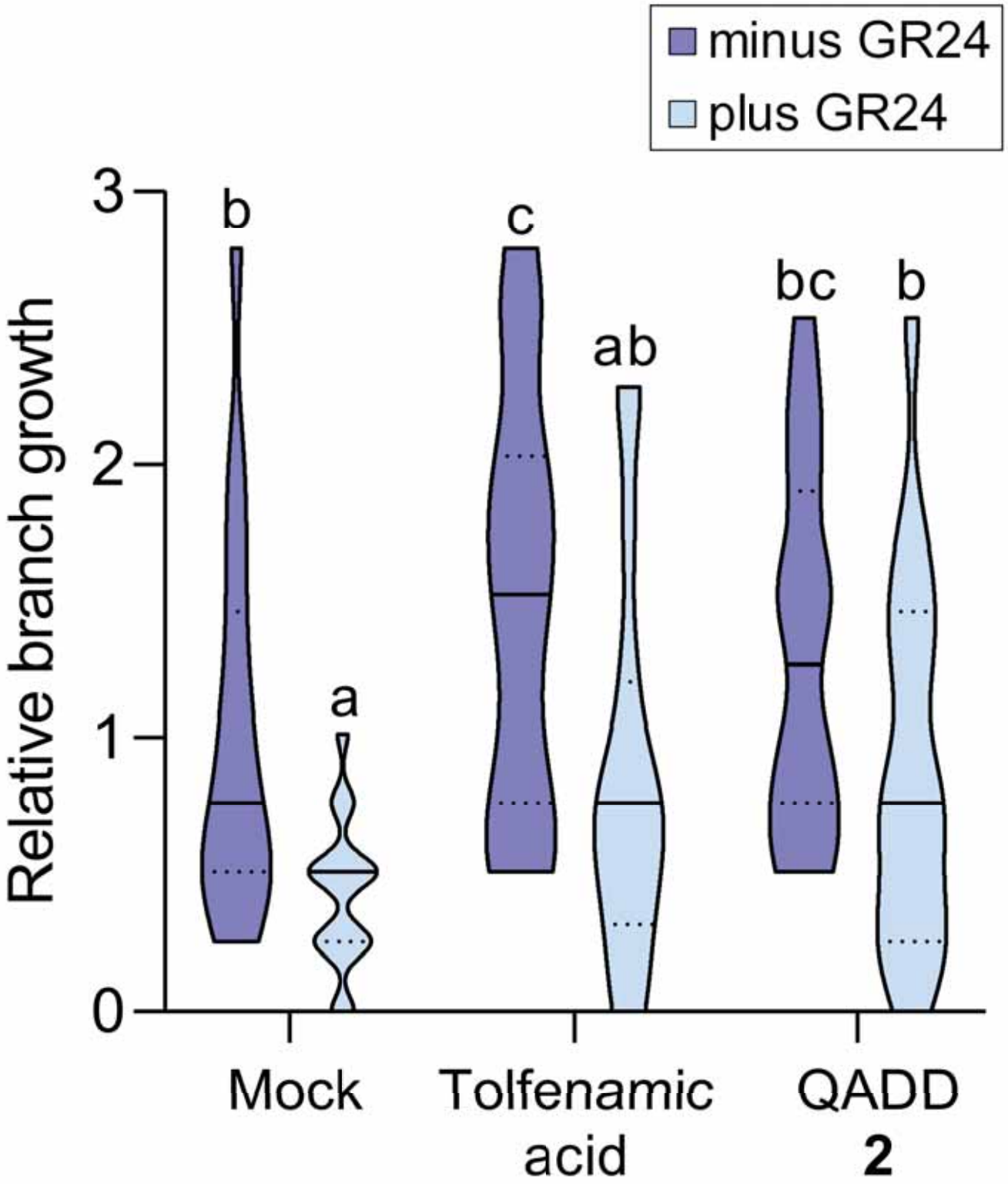
minus GR24
plus GR24
Relative branch growth
3
2
1
0
b
a
c
ab
bc
b
Mock
Tolfenamic acid
QADD 2